The Journal of Physical Chemistry Letters

pubs.acs.org/JPCL Letter

Modulating Charge Carrier Dynamics and Transfer via Surface Modifications in Organometallic Halide Perovskite Quantum Dots

William G. Delmas, Evan T. Vickers, Albert C. DiBenedetto, Calista Lum, Isaak N. Hernandez, Jin Z. Zhang,* and Sayantani Ghosh*

Cite This: *J. Phys. Chem. Lett.* 2020, 11, 7886−7892 Read Online

ABSTRACT: We investigate the effect of functionalization by acid/amine combinations of four aromatic capping ligands on the optoelectronic properties of $CH_3NH_3PbBr_3$ perovskite quantum dots (PQDs). These include benzoic acid (BA), phenylacetic acid (PAA), benzylamine, and isopropyl benzylamine. We observe that charge transfer efficiency in PQD films comprising BA-ligated samples varies between 12% and 95% as the dot density is tuned from 10^2 to 10^5 dots/μm^2 but is consistently ∼92% over that entire range for PAA-ligated PQDs. As temperature T decreases, initially, recombination is dominated by bound or trapped excitons, but below 80 K, spectral broadening, accompanied by free excitonic behavior, is observed. Our results indicate enhanced charge delocalization at lower values of T, which reduces the level of exciton confinement and recombination decay rates and underlines the importance of investigating PQD−ligand interactions at a fundamental level given the significant effect minute changes in ligand structures have on the optoelectronic properties of quantum dots.

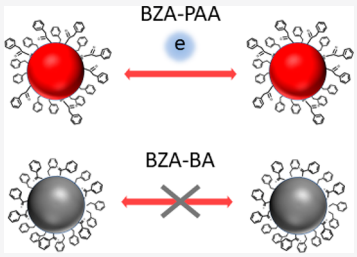

Organometallic halide perovskites (OMHPs) are currently one of the most intensively investigated materials due to their stellar success as candidates for photovoltaics.[1−4] Within a decade, the photon conversion efficiency of perovskite thin-film solar cells has increased from 3.8% to >25%,[5] which, coupled with their solution-based processing,[6,7] lightweight nature, and flexibility,[1,2] enhances their appeal greatly. In addition, OMHPs possess several unique characteristics, including a high mobility,[8−10] a large spectral absorption,[11−13] a high photoluminescence quantum yield (PLQY),[14−16] structural phase transitions, and anomalous spectral shifts with temperature.[9] Consequently, this makes them attractive semiconducting materials to investigate from a fundamental perspective, especially in the case of perovskite quantum dots (PQDs), where these qualities are combined with size tunability.[17,18] PQDs are also distinct from II−VI and III−V colloidal QDs due to their significantly smaller excitonic Bohr radius,[19] causing the PQD bandgap to be weakly dependent on PQD size.[20] Thus, there is less size inhomogeneity-induced broadening in the PL spectra for an ensemble.[21] Furthermore, the bandgap can be varied by other methods, including composition[22] and surface functionalization,[17] allowing for additional tunability options. All of this, coupled with high PLQY and long recombination lifetimes, has led to PQDs being studied for application in a wide range of devices, from photovoltaics[23−25] to light-emitting diodes,[26,27] photodetectors,[28,29] and single-photon sources.[30,31]

Initial efforts in this regard were only moderately successful[32] due to incomplete surface passivation and poor charge transport in close-packed PQD films. Like all colloidal QDs, PQDs have charge trap states on their surfaces that need to be passivated to minimize trap-related recombination.[33−35] Typically used long chain and/or branched aliphatic ligands have proven to be successful in reducing this surface trap state density,[36,37] in addition to tuning PQD size by altering synthesis conditions,[36] and in modifying the crystalline structural phase.[37] This last aspect is of particular interest as PQDs undergo a transition from the room-temperature tetragonal phase to an orthorhombic phase in the range of 110−140 K, upon which the charge recombination time and photon conversion efficiency are both significantly decreased.[38] A recent study has demonstrated that stabilizing the high-temperature phase in inorganic $CsPbI_3$ QDs significantly increased their effectiveness as room-temperature-stable photovoltaic cells.[39] Despite these benefits, the drawback to using long chain-saturated hydrocarbons and alkoxysilanes is that as insulating ligands, they hinder interdot charge transfer and transport. The use of aromatic capping ligands is one of the steps toward overcoming this problem. However, while a vast and varied library of ligands can be used in trial-and-error mode to achieve improved functionality with respect to a specific application, investigation of the fundamental aspects of how ligands influence the optoelectronic properties of the PQDs will offer a faster optimization route, allowing for

Received: July 14, 2020
Accepted: September 1, 2020
Published: September 1, 2020

https://dx.doi.org/10.1021/acs.jpclett.0c02151
J. Phys. Chem. Lett. 2020, 11, 7886−7892

rational design. In this work, we investigate the effect of using acid/amine combinations of four different aromatic capping ligands on the optoelectronic properties of $CH_3NH_3PbBr_3$ PQDs. The ligands containing both conjugated and non-conjugated components include benzoic acid (BA), phenylacetic acid (PAA), benzylamine (BZA), and isopropyl benzylamine (IPBZA). Using temperature- and power-dependent ultrafast spectroscopy, we demonstrate that small differences in the chemical properties of the ligands strongly affect other properties of the PQDs.

Figure 1A shows the molecular structures of the capping ligands used in our study. BA is a fully conjugated structure,

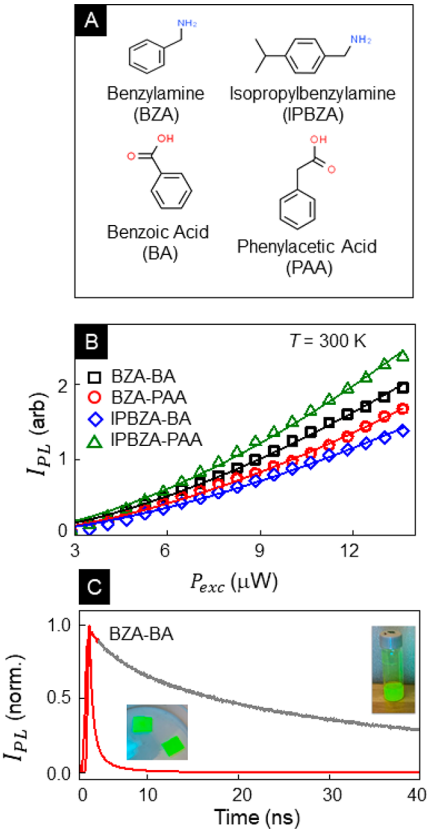

Figure 1. (A) Chemical structures of the molecular components used to design the capping ligands. (B) PL intensity I_{PL} of the differently functionalized PQD films varying with excitation power P_{exc}. Fits are to a power law. (C) Time-resolved PL of BZA-BA PQDs in solution and in film.

and BZA, IPBZA, and PAA are partially conjugated (Figure S1). Combinations of amines BZA and IPBZA with acids BA and PAA are designed to achieve proton transfer from the acids to the amines, resulting in carboxylate (R-COO$^-$) and ammonium (R′-NH$_3^+$) to passivate positive and negative surface defects of the PQDs.[40] We begin by assessing the room-temperature optical properties of the PQDs. PL emission is centered between 529 and 532 nm (Figure S2), a minor variation. PLQY is an excellent measure of how well each combination passivates the PQD surfaces,[33,34] and the PLQYs for BZA-PAA, BZA-BA, IPBZA-PAA, and IPBZA-BA are 24%, 21%, 17%, and 15%, respectively, measured in PQD films. Prior work has shown that in solution the PLQY of BZA-BA PQDs is ∼80%.[40] The quenched yield in films could be due to interaction between PQDs or due to the quenching effect from the surface of the substrate. We verified that this effect is not substrate-related, having observed the quenched yield on both silicon and glass, and conclude that increased nonradiative processes arising from interdot energy or charge transfer are responsible. Figure 1B shows the spectrally integrated PL intensity I_{PL} as a function of excitation power P_{exc}. A power law $I_{PL} = \alpha P_{exc}^{\ k}$ is fit to the data (α is a normalization constant) to determine the nature of charge carriers.

In direct bandgap semiconductors, a k of >2 indicates recombination dominated by free electron−hole pairs, a k between 1 and 2 indicates recombination dominated by a mixture of free and bound excitons, and a k of <1 results from bound excitons.[41−46] The spatial confinement of PQDs generally leads to bound excitonic recombination.[37,38] The fits return k values between 1.52 and 1.56 for the four populations, indicating the presence of free excitons, suggesting a modification of the exciton wave function, similar to what has been observed in CdSe/ZnS QDs.[47] Figure 1C shows time-resolved photoluminescence (TRPL) curves of I_{PL} for BZA-BA PQDs suspended in a toluene solution and deposited as a film. The recombination time in solution, extracted from a single-exponential fit, is 47 ns and ranges between 47 and 50 ns for the other PQDs. These are much longer than those of $CH_3NH_3PbBr_3$ QDs functionalized with insulating ligands.[37] In the PQD film, the decay is much faster, and a biexponential function ($I_{PL} = A_1e^{-t/\tau_1} + A_2e^{-t/\tau_2}$) is required to fit the TRPL curve, from which we extract an average lifetime, defined as $\tau_{av} = [(A_1\tau_1)^2 + (A_2\tau_2)^2]/(A_1\tau_1 + A_2\tau_2)$. It is typical for recombination in solutions with isolated particles to have a single rate and is a confirmation that the effects of defect or traps states are negligible. The emergence of a second time scale in the PQD film is an indication of another recombination route becoming available. Discerning which time scale arises from what recombination channel is not a straightforward matter, as additional mechanisms often convolute the entire process. There is an extensive body of literature that discusses these additional routes.[48−50] However, it is well-established that Förster resonance energy transfer (FRET), which drives the transfer of energy from donors to acceptors, is a common mechanism that is responsible for such an effect in quantum dot films. Smaller QDs in an ensemble emitting at shorter wavelengths act as donors and transfer energy to the larger ones (acceptors).[51,52] The consequence is a distribution of the recombination lifetimes across the emission spectrum. The QDs emitting at the shortest wavelengths have the fastest recombination lifetime, and this trend continues, with the lifetime increasing monotonically with emission wavelength. At the long wavelength tail, the recombination lifetime approaches the value of that measured in solution. In our samples, τ_{av} in the PQD films is not only much smaller than the solution lifetime but also nearly invariant across the spectrum. As an example, in the BZA-BA PQDs, τ_{av} ranges between 1.7 and 2 ns from the shortest to the longest emission wavelength, and in BZA-PAA PQDs, $\tau_{av} \sim 6$ ns over the same range (Figure S3A,B). In addition, the relative intensities of the two components remain unchanged across the emission spectra, as well (Figure S3C,D). We thus confirm that the faster recombination in PQD films does not originate from FRET. The remaining option is charge transfer, which we investigate next.

Figure 2A depicts a collection of TRPL curves for PQDs functionalized with BZA-BA (top) and IPBZA-PAA (bottom) at different dot densities in films, which were estimated using

https://dx.doi.org/10.1021/acs.jpclett.0c02151
J. Phys. Chem. Lett. 2020, 11, 7886−7892

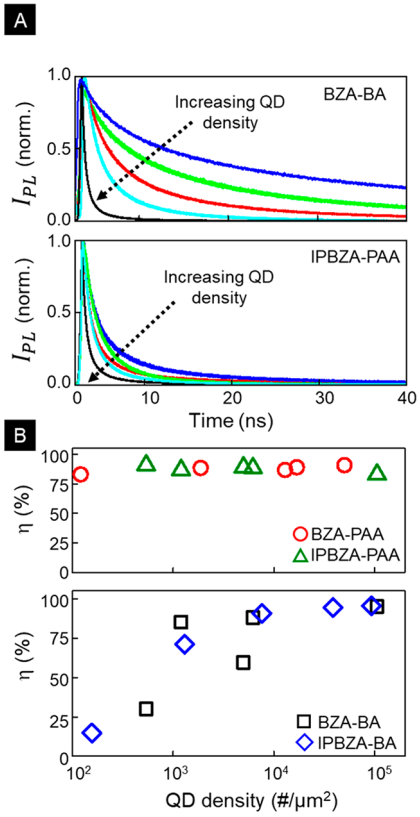

Figure 2. (A) Time-resolved PL of (top) BZA-BA and (bottom) IPBZA-PAA PQD films of varying dot areal density. (B) Charge transfer efficiency η for all PQD films varying with dot density.

PL and PLQY measurements. We extract the average lifetime τ_{av} and observe that while for BZA-BA PQDs, τ_{av} decreases continuously with an increase in PQD density, the changes in recombination rates for IPBZA-PAA-ligated PQDs over the same range are negligible. The same trends are observed in IPBZA-BA (gradual change) and BZA-PAA (none) PQDs with PQD density. To quantify the charge transfer, we calculate an efficiency $\eta \equiv 1 - \tau_{av}/\tau_s$, where τ_{av} and τ_s are the measured average lifetimes in films and in solution, respectively. Plotted in Figure 2B, η is nearly constant at 92% for BZA-PAA and IPBZA-PAA over the entire density range. The BA-ligated PQDs mildly outperform the PAA-functionalized dots at concentrations of >10^4 dots/μm^2, with $\eta \sim 95\%$ in the most densely packed films, but demonstrate weak charge transfer at low densities. This variation may be due to PAA being longer, which could allow efficient charge transfer at low densities. We have also compared the relative intensities of the two time scales in the biexponential fits (Figure S4A,B). In the BA-ligated PQD films, at low densities the two time scales are very different (50 and 7 ns), and the longer one accounts for nearly 70% of the total decay. As the PQD density increases, this longer lifetime and its relative contribution rapidly decrease, until in the densest film, it accounts for only 4% of the signal. The short lifetime also decreases, to 2 ns, but its enhanced intensity leads us to assign this one as a measure of the charge transfer process, while the longer time scale reflects radiative recombination. This latter is also affected as charge transfer becomes more efficient. In sharp contrast, while the PAA-functionalized PQDs have two time scales in the TRPL data, they are less disparate (11 and 3 ns). More importantly, the longer time accounts for only 4% at all densities, including the lowest one. Finally, we note that at the highest density of 10^5 dots/μm^2, the time scales in both types of PQDs converge to ~10 and 2 ns, underlining the essential similarity of the charge transfer processes that determine them.

In addition to room-temperature studies, we investigate the temperature-dependent behavior of the different competitive dynamical processes. In Figure 3, we map I_{PL} with emission wavelength λ and temperature T for BZA-BA PQDs. $CH_3NH_3PbBr_3$ QDs undergo a transition from a tetragonal to an orthorhombic phase between 100 and 140 K, which results in an increased bandgap and a significantly faster recombination rate.[37] Figure 3A shows a single emission peak over the entire temperature range, indicating no transition to the orthorhombic phase. The emission centered around 530 nm at 300 K red-shifts with a decrease in T. This is common in perovskites,[4] including PQDs. However, there is a distinct kink in the map where the red-shift abruptly acquires a different slope. We label this temperature T_1. In addition, as Figure 3B demonstrates, the spectral fwhm narrows as T decreases, as homogeneous broadening is suppressed with decreasing phonon contributions, but the spectral width starts to increase again at a temperature we label T_2. τ_{av} remains unchanged until T = 150 K, indicating a persistent high charge transfer efficiency (Figure S5A). Figure 3C plots the emission spectra at 90 and 30 K, and the increase in fwhm between the two is noticeable. For all spectra below 90 K, we decompose the curves into two distributions, denoting the low-wavelength

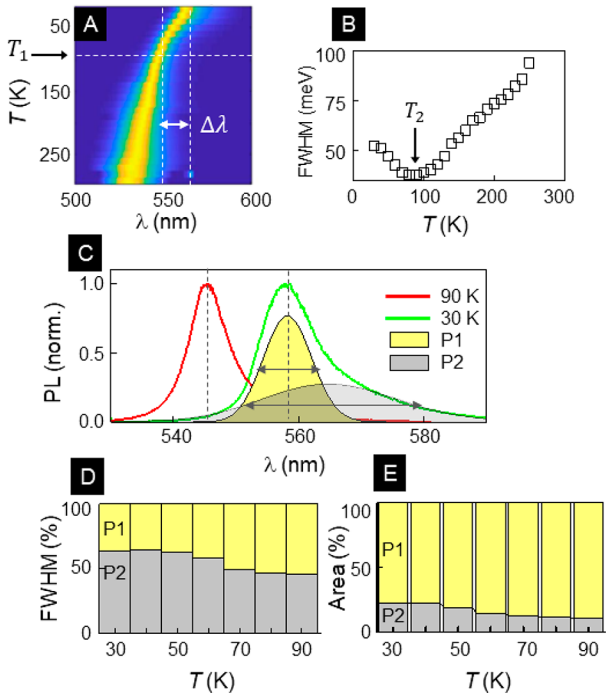

Figure 3. (A) PL emission intensity mapped with T and emission wavelength λ for BZA-BA PQDs. T_1 denotes the temperature where the slope change occurs, and $\Delta\lambda$ is the spectral shift at $T < T_1$. (B) Full width at half-maximum (fwhm) plotted with T. The temperature at which the fwhm has a minimum is labeled as T_2. (C) PL emission spectra at different T values highlighting the related red-shift and spectral width variations. Spectra below 90 K are fit with two peaks, as shown for the emission curve at 30 K. Relative weights of (D) fwhm and (E) spectrally integrated intensity of the two peaks varying with T.

https://dx.doi.org/10.1021/acs.jpclett.0c02151
J. Phys. Chem. Lett. 2020, 11, 7886−7892

contribution P1, and identify that as the exciton peak. The second longer wavelength peak, P2, represents the additional channels that cause the anomalous spectral broadening. In panels D and E of Figure 3, we plot the relative contributions of P1 and P2 to the fwhm and the spectrally integrated PL, respectively, and show that the contribution from P2 increases with a decrease in T. By 60 K, more than 50% of the spectral width is due to the longer wavelength emission. The characterization of I_{PL} with excitation power at room temperature in Figure 1B shows the presence of both free and bound/trapped excitons. In Figure 4A, we see at 210 K the

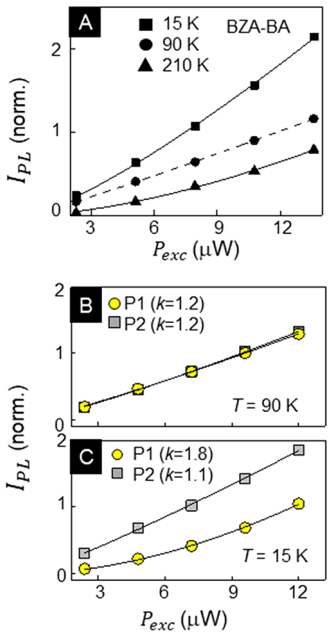

Figure 4. (A) PL emission of BZA-BA-functionalized PQD films at 15, 90, and 210 K varying with excitation power. PL intensity I_{PL} acquired from fits to emission spectra as discussed in Figure 3 at (B) 15 K and (C) 90 K. I_{PL} is plotted separately for peaks P1 and P2 as labeled in Figure 3.

fit $I_{PL} = \alpha P_{exc}^{k}$ returns $k = 1.58$, indicating the presence of both excitonic populations, just like at room temperature. At 90 K, $k = 1.08$, implying recombination is driven by bound or trapped excitons. This is what is expected with a decrease in temperature, but at 15 K, we see I_{PL} becoming nonlinear again, with $k = 1.3$. This is unexpected, so we perform this fit on the P1 and P2 parts of the emission spectra separately. At 90 K in Figure 4B, both P1 and P2 have a nearly linear dependence on excitation power, but in Figure 4C at 15 K, P1, the excitonic contribution, appears almost quadratic with $k = 1.8$. The power dependence of P2 remains nearly linear, which means the reversed trend in k observed in Figure 4A is not from the longer wavelength portion that drives the spectral broadening, but from the presence of free excitonic contributions again, an unusual feature at low temperatures.

Before delving into this further, we summarize the temperature-dependent behavior of PQDs functionalized with the other ligands. PL maps of BZA-PAA, IPBZA-PAA PQDs (Figure S6), and IPBZA-BA (Figure S7) all show the increased spectral red-shift at low temperatures. The fwhm's of PAA-ligated PQDs are plotted with T in panels A and B of Figure 5, which show that the fwhm's of BZA-PAA PQDs show nearly no increase in the low-temperature region. In

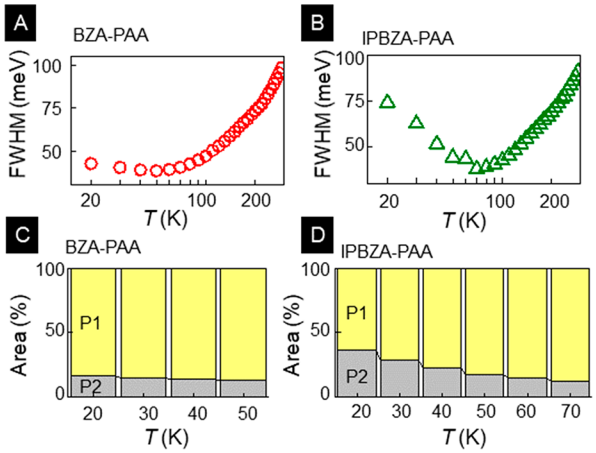

Figure 5. fwhm of (A) BZA-PAA and (B) IPBZA-PAA PQDs varying with T. Relatives weights of the low-wavelength (P1) and high-wavelength (P2) components of the low-temperature spectra for (C) BZA-PAA and (D) IPBZA-PAA PQDs.

contrast, the broadening is significant in IPBZA-PAA PQDs, with the fwhm at 20 K being almost as large as at room temperature. An additional difference shows up in panels C and D of Figure 5. BZA-PAA emission has a small contribution from the long wavelength tail (P2), which remains nearly constant with T, whereas in IPBZA-PAA, those same states have a more significant effect. Table 1 summarizes the key

Table 1. Overall Spectral Red-Shifts with a Decrease in T, Critical Points for the Red-Shift Kink, Critical Points for the Change in fwhm, and PQD PLQYs for Each of the Four PQD Types

composition	$\Delta\lambda$ (meV)	T_1 (K)	T_2 (K)	PLQY (%)
BZA-BA	120	100	85	20
BZA-PAA	100	108	50	24
IPBZA-BA	120	104	68	15
IPBZA-PAA	120	102	77	17

parameters that characterize the low-temperature behavior of the PQDs. These include $\Delta\lambda$, the spectral peak red-shift after the slope change, as shown in Figure 3A; T_1, the temperature where this slope change begins, also labeled in Figure 3A; and T_2, the temperature where the spectral fwhm begins to increase, labeled in Figure 3B, which is also where the recombination lifetimes begin to decrease (Figure S4). The tabulation underlines the fact that while $\Delta\lambda$ and T_1 are very similar for all of the PQDs, irrespective of the ligand composition, T_2 is not. In addition, T_2 is the lowest for BZA-PAA PQDs, which also have the highest PLQY. On the basis of these observations, it seems that the low-temperature behavior has two contributing factors: one that causes spectral broadening and faster recombination, which is related to the PLQY, and a second independent factor that drives the spectral shift. The latter affects all of the PQDs in the same way, resulting in the nearly identical values of $\Delta\lambda$ and T_1.

We schematically depict these mechanisms in Figure 6. The first, shown in Figure 6A, is related to the presence of trap states within the PQD bandgap, with ΔE situated below the conduction band. When $T > \Delta E/k_B$, where k_B is the Boltzmann constant, excitons have adequate thermal energy to escape the trap states and return to the conduction band and undergo

https://dx.doi.org/10.1021/acs.jpclett.0c02151
J. Phys. Chem. Lett. 2020, 11, 7886−7892

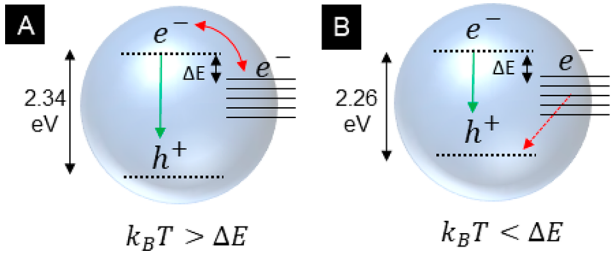

Figure 6. Schematic depicting trap states in the bandgap, ΔE situated below the conduction band, and the related recombination channels for (A) $k_BT > \Delta E$ and (B) $k_BT < \Delta E$.

direct recombination at the band edge. When $T \leq \Delta E/k_B$, the carriers are trapped, driving trap-assisted recombination in the form of the second, low-energy peak P2. This also results in the increased spectral fwhm, as there is now an additional channel of recombination available. If $T_2 = \Delta E/k_B$, ΔE ranges from 4.3 to 7 meV based on the spread of T_2 values. These trap states originate in surface defects, which aligns well with the observation that both T_2 and the related spectral changes vary considerably among the four PQD samples. It also explains why the combination of the ligand with the smallest fwhm increases and the lowest T_2 is BZA-PAA, with the highest PLQY. The defect trap states cannot explain the abrupt shift observed at T_1, which is consistent with all of the PQDs. The defect trap states also cannot explain the change in the nature of excitonic recombination observed when $T < T_1$ shown in Figure 4.

We speculate that this shift observed at T_1 is driven by the ligands themselves. Structurally, at room temperature, the ligands are in a constant state of fluctuation, adopting different conformations or configurations with respect to the PQD surface and with respect to each other for ligands from different PQDs (Figure S8). As T decreases, the ligands relax into their most stable conformation. It is possible that while this relaxation occurs, the ligands condense into a coupling geometry depicted in Figure S8B, where the two benzene rings from two ligands of two different PQDs overlap better, resulting in an increased level of delocalization of the excitonic wave function within the PQDs. Given the similarities of the ligand structures, it is likely that this would occur at the same temperature for all PQDs. It is this that manifests as a reduced bandgap and red-shifted emission because the effect is akin to decreased quantum confinement. In addition, this would also explain why the recombination would appear to have a contribution of "free" excitons for $T < T_1$ as shown in Figure 4C.

Our investigation of $CH_3NH_3PbBr_3$ PQDs functionalized with different aromatic ligands highlights how small variations in their chemical structures can cause significant differences in their static and dynamic optoelectronic properties. It also underlines the importance of extending the characterization to low temperatures, when the energy scales allow several competitive processes to come into play, thereby revealing both differences and similarities driven by the ligand structures that would otherwise not be observable. The results discussed here confirm that rationally designed aromatic ligands can serve the dual purpose of highly effective surface passivation and allowing efficient charge transfer, without any detrimental effects on the native spectral properties of the PQDs. In particular, the consistently high charge transfer efficiency η in PAA-ligated PQDs over a broad density range indicates these could potentially be well-suited for use in QD-film-based devices. The fact that the recombination properties are stable down to 100 K for most of the PQDs is another point in favor of their application in situations where thermal cycling may be a possibility, therefore broadening the scope of utilization of these novel nanomaterials.

■ EXPERIMENTAL METHODS

Synthesis. $CH_3NH_3PbBr_3$ PQDs were synthesized following procedures used previously.[40] The average PQD sizes for these samples were 6.2 ± 1.5 nm.[40] PQD films were fabricated by dynamic drop-casting of 2.0 mL of a PQD solution at 5.0 mol/L in toluene over 2 min spinning at 2000 rpm.

PLQY. The photoluminescence quantum yield (PLQY) was measured using a Newport 819C-SF-4 Integrating Sphere and a continuous wave 405 nm diode laser (Coherent Inc.) as the source.

PL. For spectrally resolved PL, a 100× objective was used for both excitation and collection, in a custom-designed confocal scanning PL setup. The excitation source was an NKT Photonics SuperK laser, with spectral tunability from 400 to 700 nm and a variable repetition rate between 77.5 and 5.56 MHz. After collection, the emission was dispersed by a Princeton Scientific 250i spectrometer and then measured via a thermoelectrically cooled CCD, with a spectral resolution of 0.18 nm.

TRPL. For the time-resolved PL measurements, the signal was dispersed onto the spectrometer and then collected by a single-photon avalanche diode for analysis by a PicoQuant time-correlated single-photon counting system, with an instrument response function of 28 ps.

Temperature-Dependent Measurements. Temperature-dependent PL and TRPL were recorded using an Advanced Research Systems cryo-free, temperature-controlled Crysostat. The sample was mounted on a stage in a vacuum chamber, and the temperature was varied from 20 to 300 K in 10 K steps. The initial cooldown allowed better thermal equilibration when measurements were being taken. As the temperature was increased starting at 20 K, at each new set temperature we waited 20 min for the sample to equilibrate prior to initiating data acquisition.

■ ASSOCIATED CONTENT

Supporting Information

The Supporting Information is available free of charge at https://pubs.acs.org/doi/10.1021/acs.jpclett.0c02151.

Description of ligand chemical and resonance structures, PL spectra for the four PQD samples, demonstration of the absence of FRET in the system, analysis of recombination in PQD films for representative BA- and PAA-ligated PQDs, TRPL data for the PQD samples, PL maps of BZA-PAA and IPBZA-PAA, properties of the IPBZA-BA sample, and illustration of a possible low-temperature exciton delocalization route (PDF)

■ AUTHOR INFORMATION

Corresponding Authors

Jin Z. Zhang − *Department of Chemistry and Biochemistry, University of California, Santa Cruz, California 95064, United States;* orcid.org/0000-0003-3437-912X; Email: zhang@ucsc.edu

https://dx.doi.org/10.1021/acs.jpclett.0c02151
J. Phys. Chem. Lett. 2020, 11, 7886−7892

Sayantani Ghosh − *Department of Physics, School of Natural Sciences, University of California, Merced, California 95344, United States;* orcid.org/0000-0003-3440-7194; Email: sghosh@ucmerced.edu

Authors

William G. Delmas − *Department of Physics, School of Natural Sciences, University of California, Merced, California 95344, United States;* orcid.org/0000-0002-6030-0318

Evan T. Vickers − *Department of Chemistry and Biochemistry, University of California, Santa Cruz, California 95064, United States;* orcid.org/0000-0002-9594-4279

Albert C. DiBenedetto − *Department of Physics, School of Natural Sciences, University of California, Merced, California 95344, United States*

Calista Lum − *Department of Physics, School of Natural Sciences, University of California, Merced, California 95344, United States*

Isaak N. Hernandez − *Department of Physics, Massachusetts Institute of Technology, Cambridge, Massachusetts 02139, United States*

Complete contact information is available at: https://pubs.acs.org/10.1021/acs.jpclett.0c02151

Author Contributions

W.G.D. performed all measurements and led data analysis efforts. E.T.V. synthesized all samples. A.C.D., C.L., and I.N.H. assisted W.G.D. in data acquisition and analysis. J.Z.Z. and S.G. supervised all characterization and measurements.

Notes

The authors declare no competing financial interest.

■ ACKNOWLEDGMENTS

This work was possible through the support of NASA MIRO Grant NNX15AQ01A.

■ ABBREVIATIONS

BA, benzoic acid; PAA, phenylacetic acid; BZA, benzylamine; IPBZA, isopropyl benzylamine; PLQY, photoluminescence quantum yield; PQD, perovskite quantum dot; OA, octylamine; OABr, octylaminebromide; APTES, 3-aminopropyl triethoxysilane; TRPL, time-resolved photoluminescence; FRET, Förster resonance energy transfer; fwhm, full width at half-maximum

■ REFERENCES

(1) Palmstrom, A. F.; Eperon, G. E.; Leijtens, T.; Prasanna, R.; Habisreutinger, S. N.; Nemeth, W.; Gaulding, E. A.; Dunfield, S. P.; Reese, M.; Nanayakkara, S.; Moot, T.; Werner, J.; Liu, J.; To, B.; Christensen, S. T.; McGehee, M. D.; van Hest, M. F. A. M.; Luther, J. M.; Berry, J. J.; Moore, D. T. Enabling Flexible All-Perovskite Tandem Solar Cells. *Joule* **2019**, *3* (9), 2193−2204.

(2) Jung, H. S.; Han, G. S.; Park, N. G.; Ko, M. J. Flexible Perovskite Solar Cells. *Joule* **2019**, *3* (8), 1850−1880.

(3) Yang, Z.; Zhang, S.; Li, L.; Chen, W. Research Progress on Large-Area Perovskite Thin Films and Solar Modules. *J. Mater.* **2017**, *3* (4), 231−244.

(4) Yin, W. J.; Yang, J. H.; Kang, J.; Yan, Y.; Wei, S. H. Halide Perovskite Materials for Solar Cells: A Theoretical Review. *J. Mater. Chem. A* **2015**, *3* (17), 8926−8942.

(5) Best Research-Cell Efficiency Chart|Photovoltaic Research|. National Renewable Energy Laboratory. https://www.nrel.gov/pv/cell-efficiency.html (accessed 2019-08-05).

(6) Zhang, F.; Zhu, K. Additive Engineering for Efficient and Stable Perovskite Solar Cells. *Adv. Energy Mater.* **2020**, *10* (13), 1902579.

(7) Chen, W.; Li, X.; Li, Y.; Li, Y. A Review: Crystal Growth for High-Performance All-Inorganic Perovskite Solar Cells. *Energy Environ. Sci.* **2020**, *13* (7), 1971−1996.

(8) Reid, O. G.; Yang, M.; Kopidakis, N.; Zhu, K.; Rumbles, G. Grain-Size-Limited Mobility in Methylammonium Lead Iodide Perovskite Thin Films. *ACS Energy Lett.* **2016**, *1* (3), 561−565.

(9) Milot, R. L.; Eperon, G. E.; Snaith, H. J.; Johnston, M. B.; Herz, L. M. Temperature-Dependent Charge-Carrier Dynamics in $CH_3NH_3PbI_3$ Perovskite Thin Films. *Adv. Funct. Mater.* **2015**, *25* (39), 6218−6227.

(10) Lim, J.; Hörantner, M. T.; Sakai, N.; Ball, J. M.; Mahesh, S.; Noel, N. K.; Lin, Y. H.; Patel, J. B.; McMeekin, D. P.; Johnston, M. B.; Wenger, B.; Snaith, H. J. Elucidating the Long-Range Charge Carrier Mobility in Metal Halide Perovskite Thin Films. *Energy Environ. Sci.* **2019**, *12* (1), 169−176.

(11) Yuan, H.; Zhao, Y.; Duan, J.; Wang, Y.; Yang, X.; Tang, Q. All-Inorganic $CsPbBr_3$ Perovskite Solar Cell with 10.26% Efficiency by Spectra Engineering. *J. Mater. Chem. A* **2018**, *6* (47), 24324−24329.

(12) Tian, Y.; Scheblykin, I. G. Artifacts in Absorption Measurements of Organometal Halide Perovskite Materials: What Are the Real Spectra? *J. Phys. Chem. Lett.* **2015**, *6* (13), 3466−3470.

(13) Hao, F.; Stoumpos, C. C.; Chang, R. P. H.; Kanatzidis, M. G. Anomalous Band Gap Behavior in Mixed Sn and Pb Perovskites Enables Broadening of Absorption Spectrum in Solar Cells. *J. Am. Chem. Soc.* **2014**, *136* (22), 8094−8099.

(14) La-Placa, M. G.; Longo, G.; Babaei, A.; Martínez-Sarti, L.; Sessolo, M.; Bolink, H. J. Photoluminescence Quantum Yield Exceeding 80% in Low Dimensional Perovskite Thin-Films: Via Passivation Control. *Chem. Commun.* **2017**, *53* (62), 8707−8710.

(15) Wang, Z.; Wang, F.; Sun, W.; Ni, R.; Hu, S.; Liu, J.; Zhang, B.; Alsaed, A.; Hayat, T.; Tan, Z. Manipulating the Trade-off Between Quantum Yield and Electrical Conductivity for High-Brightness Quasi-2D Perovskite Light-Emitting Diodes. *Adv. Funct. Mater.* **2018**, *28* (47), 1804187.

(16) Sutter-Fella, C. M.; Li, Y.; Amani, M.; Ager, J. W.; Toma, F. M.; Yablonovitch, E.; Sharp, I. D.; Javey, A. High Photoluminescence Quantum Yield in Band Gap Tunable Bromide Containing Mixed Halide Perovskites. *Nano Lett.* **2016**, *16* (1), 800−806.

(17) Bai, Z.; Zhong, H. Halide Perovskite Quantum Dots: Potential Candidates for Display Technology. *Sci. Bull.* **2015**, *60* (18), 1622−1624.

(18) Luo, B.; Pu, Y.-C.; Lindley, S. A.; Yang, Y.; Lu, L.; Li, Y.; Li, X.; Zhang, J. Z. Organolead Halide Perovskite Nanocrystals: Branched Capping Ligands Control Crystal Size and Stability. *Angew. Chem., Int. Ed.* **2016**, *55* (31), 8864−8868.

(19) Tilchin, J.; Dirin, D. N.; Maikov, G. I.; Sashchiuk, A.; Kovalenko, M. V.; Lifshitz, E. Hydrogen-like Wannier-Mott Excitons in Single Crystal of Methylammonium Lead Bromide Perovskite. *ACS Nano* **2016**, *10* (6), 6363−6371.

(20) Castañeda, J. A.; Nagamine, G.; Yassitepe, E.; Bonato, L. G.; Voznyy, O.; Hoogland, S.; Nogueira, A. F.; Sargent, E. H.; Cruz, C. H. B.; Padilha, L. A. Efficient Biexciton Interaction in Perovskite Quantum Dots under Weak and Strong Confinement. *ACS Nano* **2016**, *10* (9), 8603−8609.

(21) Utzat, H.; Shulenberger, K. E.; Achorn, O. B.; Nasilowski, M.; Sinclair, T. S.; Bawendi, M. G. Probing Linewidths and Biexciton Quantum Yields of Single Cesium Lead Halide Nanocrystals in Solution. *Nano Lett.* **2017**, *17* (11), 6838−6846.

(22) Yang, G. L.; Zhong, H. Z. Organometal Halide Perovskite Quantum Dots: Synthesis, Optical Properties, and Display Applications. *Chin. Chem. Lett.* **2016**, *27* (8), 1124−1130.

(23) Ling, X.; Zhou, S.; Yuan, J.; Shi, J.; Qian, Y.; Larson, B. W.; Zhao, Q.; Qin, C.; Li, F.; Shi, G.; Stewart, C.; Hu, J.; Zhang, X.; Luther, J. M.; Duhm, S.; Ma, W. 14.1% $CsPbI_3$ Perovskite Quantum Dot Solar Cells via Cesium Cation Passivation. *Adv. Energy Mater.* **2019**, *9* (28), 1900721.

(24) Liu, F.; Zhang, Y.; Ding, C.; Kobayashi, S.; Izuishi, T.; Nakazawa, N.; Toyoda, T.; Ohta, T.; Hayase, S.; Minemoto, T.; Yoshino, K.; Dai, S.; Shen, Q. Highly Luminescent Phase-Stable $CsPbI_3$ Perovskite Quantum Dots Achieving Near 100% Absolute Photoluminescence Quantum Yield. *ACS Nano* **2017**, *11* (10), 10373−10383.
(25) Xue, J.; Wang, R.; Chen, L.; Nuryyeva, S.; Han, T.; Huang, T.; Tan, S.; Zhu, J.; Wang, M.; Wang, Z.; Zhang, C.; Lee, J.; Yang, Y. A Small-Molecule "Charge Driver" Enables Perovskite Quantum Dot Solar Cells with Efficiency Approaching 13%. *Adv. Mater.* **2019**, *31* (37), 1900111.
(26) Li, Y.; Chou, S.; Huang, P.; Xiao, C.; Liu, X.; Xie, Y.; Zhao, F.; Huang, Y.; Feng, J.; Zhong, H.; Sun, H.; Pei, Q. Quantum Dot LEDs: Stretchable Organometal-Halide-Perovskite Quantum-Dot Light-Emitting Diodes. *Adv. Mater.* **2019**, *31* (22), 1970157.
(27) Yun, H.-S.; Noh, K.; Kim, J.; Noh, S. H.; Kim, G.-H.; Lee, W.; Na, H. B.; Yoon, T.-S.; Jang, J.; Kim, Y.; Cho, S.-Y. $CsPbBr_3$ Perovskite Quantum Dot Light-Emitting Diodes Using Atomic Layer Deposited Al_2O_3 and ZnO Interlayers. *Phys. Status Solidi RRL* **2020**, *14* (1), 1900573.
(28) Zhou, L.; Yu, K.; Yang, F.; Zheng, J.; Zuo, Y.; Li, C.; Cheng, B.; Wang, Q. All-Inorganic Perovskite Quantum Dot/Mesoporous TiO_2 Composite-Based Photodetectors with Enhanced Performance. *Dalt. Trans.* **2017**, *46* (6), 1766−1769.
(29) Wu, H.; Si, H.; Zhang, Z.; Kang, Z.; Wu, P.; Zhou, L.; Zhang, S.; Zhang, Z.; Liao, Q.; Zhang, Y. All-Inorganic Perovskite Quantum Dot-Monolayer MoS_2 Mixed-Dimensional van Der Waals Heterostructure for Ultrasensitive Photodetector. *Adv. Sci.* **2018**, *5* (12), 1801219.
(30) Utzat, H.; Sun, W.; Kaplan, A. E. K.; Krieg, F.; Ginterseder, M.; Spokoyny, B.; Klein, N. D.; Shulenberger, K. E.; Perkinson, C. F.; Kovalenko, M. V.; Bawendi, M. G. Coherent Single-Photon Emission from Colloidal Lead Halide Perovskite Quantum Dots. *Science* **2019**, *363* (6431), 1068−1072.
(31) Tang, X.; Hu, Z.; Chen, W.; Xing, X.; Zang, Z.; Hu, W.; Qiu, J.; Du, J.; Leng, Y.; Jiang, X.; Mai, L. Room Temperature Single-Photon Emission and Lasing for All-Inorganic Colloidal Perovskite Quantum Dots. *Nano Energy* **2016**, *28*, 462−468.
(32) Sutherland, B. R.; Sargent, E. H. Perovskite Photonic Sources. *Nat. Photonics* **2016**, *10* (5), 295−302.
(33) Lim, S. J.; Ma, L.; Schleife, A.; Smith, A. M. Quantum Dot Surface Engineering: Toward Inert Fluorophores with Compact Size and Bright. *Coord. Chem. Rev.* **2016**, *320−321*, 216−237.
(34) Schneider, R.; Weigert, F.; Lesnyak, V.; Leubner, S.; Lorenz, T.; Behnke, T.; Dubavik, A.; Joswig, J. O.; Resch-Genger, U.; Gaponik, N.; Eychmüller, A. PH and Concentration Dependence of the Optical Properties of Thiol-Capped CdTe Nanocrystals in Water and D2O. *Phys. Chem. Chem. Phys.* **2016**, *18* (28), 19083−19092.
(35) Abbandonato, G.; Hoffmann, K.; Resch-Genger, U. Determination of Quantum Yields of Semiconductor Nanocrystals at the Single Emitter Level: Via Fluorescence Correlation Spectroscopy. *Nanoscale* **2018**, *10* (15), 7147−7154.
(36) Luo, B.; Pu, Y. C.; Lindley, S. A.; Yang, Y.; Lu, L.; Li, Y.; Li, X.; Zhang, J. Z. Organolead Halide Perovskite Nanocrystals: Branched Capping Ligands Control Crystal Size and Stability. *Angew. Chem., Int. Ed.* **2016**, *55* (31), 8864−8868.
(37) Sarang, S.; Bonabi Naghadeh, S.; Luo, B.; Kumar, P.; Betady, E.; Tung, V.; Scheibner, M.; Zhang, J. Z.; Ghosh, S. Stabilization of the Cubic Crystalline Phase in Organometal Halide Perovskite Quantum Dots via Surface Energy Manipulation. *J. Phys. Chem. Lett.* **2017**, *8* (21), 5378−5384.
(38) Yuan, X.; Jing, P.; Li, J.; Wei, M.; Hua, J.; Zhao, J.; Tian, L.; Li, J. Temperature-Dependent Photoluminescence of Inorganic Perovskite Nanocrystal Films. *RSC Adv.* **2016**, *6* (82), 78311−78316.
(39) Swarnkar, A.; Marshall, A. R.; Sanehira, E. M.; Chernomordik, B. D.; Moore, D. T.; Christians, J. A.; Chakrabarti, T.; Luther, J. M. Quantum Dot-Induced Phase Stabilization of -CsPbI3 Perovskite for High-Efficiency Photovoltaics. *Science* **2016**, *354* (6308), 92−95.
(40) Vickers, E. T.; Enlow, E. E.; Delmas, W. G.; Dibenedetto, A. C.; Chowdhury, A. H.; Bahrami, B.; Dreskin, B. W.; Graham, T. A.; Hernandez, I. N.; Carter, S. A.; Ghosh, S.; Qiao, Q.; Zhang, J. Z. Enhancing Charge Carrier Delocalization in Perovskite Quantum Dot Solids with Energetically Aligned Conjugated Capping Ligands. *ACS Energy Lett.* **2020**, *5*, 817−825.
(41) D'Innocenzo, V.; Grancini, G.; Alcocer, M. J. P.; Kandada, A. R. S.; Stranks, S. D.; Lee, M. M.; Lanzani, G.; Snaith, H. J.; Petrozza, A. Excitons versus Free Charges in Organo-Lead Tri-Halide Perovskites. *Nat. Commun.* **2014**, *5*, 3586.
(42) Sarang, S.; Ishihara, H.; Chen, Y. C.; Lin, O.; Gopinathan, A.; Tung, V. C.; Ghosh, S. Low Temperature Excitonic Spectroscopy and Dynamics as a Probe of Quality in Hybrid Perovskite Thin Films. *Phys. Chem. Chem. Phys.* **2016**, *18* (41), 28428−28433.
(43) Deschler, F.; Price, M.; Pathak, S.; Klintberg, L. E.; Jarausch, D. D.; Higler, R.; Hüttner, S.; Leijtens, T.; Stranks, S. D.; Snaith, H. J.; Atatüre, M.; Phillips, R. T.; Friend, R. H. High Photoluminescence Efficiency and Optically Pumped Lasing in Solution-Processed Mixed Halide Perovskite Semiconductors. *J. Phys. Chem. Lett.* **2014**, *5* (8), 1421−1426.
(44) Wehrenfennig, C.; Liu, M.; Snaith, H. J.; Johnston, M. B.; Herz, L. M. Homogeneous Emission Line Broadening in the Organo Lead Halide Perovskite CH3NH3PbI3- XClx. *J. Phys. Chem. Lett.* **2014**, *5* (8), 1300−1306.
(45) DeQuilettes, D. W.; Vorpahl, S. M.; Stranks, S. D.; Nagaoka, H.; Eperon, G. E.; Ziffer, M. E.; Snaith, H. J.; Ginger, D. S. Impact of Microstructure on Local Carrier Lifetime in Perovskite Solar Cells. *Science* **2015**, *348* (6235), 683−686.
(46) Miyata, A.; Mitioglu, A.; Plochocka, P.; Portugall, O.; Wang, J. T. W.; Stranks, S. D.; Snaith, H. J.; Nicholas, R. J. Direct Measurement of the Exciton Binding Energy and Effective Masses for Charge Carriers in Organic-Inorganic Tri-Halide Perovskites. *Nat. Phys.* **2015**, *11* (7), 582−587.
(47) Jin, S.; Harris, R. D.; Lau, B.; Aruda, K. O.; Amin, V. A.; Weiss, E. A. Enhanced Rate of Radiative Decay in CdSe Quantum Dots upon Adsorption of an Exciton-Delocalizing Ligand. *Nano Lett.* **2014**, *14* (9), 5323−5328.
(48) Wang, X.; Qu, L.; Zhang, J.; Peng, X.; Xiao, M. Surface-Related Emission in Highly Luminescent CdSe Quantum Dots. *Nano Lett.* **2003**, *3* (8), 1103−1106.
(49) Shi, Y.; Wu, W.; Dong, H.; Li, G.; Xi, K.; Divitini, G.; Ran, C.; Yuan, F.; Zhang, M.; Jiao, B.; Hou, X.; Wu, Z. A Strategy for Architecture Design of Crystalline Perovskite Light-Emitting Diodes with High Performance. *Adv. Mater.* **2018**, *30* (25), 1800251.
(50) Dai, J.; Xi, J.; Li, L.; Zhao, J.; Shi, Y.; Zhang, W.; Ran, C.; Jiao, B.; Hou, X.; Duan, X.; Wu, Z. Charge Transport between Coupling Colloidal Perovskite Quantum Dots Assisted by Functional Conjugated Ligands. *Angew. Chem., Int. Ed.* **2018**, *57* (20), 5754−5758.
(51) Shcherbatyuk, G. V.; Inman, R. H.; Ghosh, S. Anomalous Photo-Induced Spectral Changes in CdSe/ZnS Quantum Dots. *J. Appl. Phys.* **2011**, *110*, No. 053518.
(52) Crooker, S. A.; Hollingsworth, J. A.; Tretiak, S.; Klimov, V. I. Spectrally Resolved Dynamics of Energy Transfer in Quantum-Dot Assemblies: Towards Engineered Energy Flows in Artificial Materials. *Phys. Rev. Lett.* **2002**, *89* (18), 186802.

https://dx.doi.org/10.1021/acs.jpclett.0c02151
J. Phys. Chem. Lett. 2020, 11, 7886−7892